

# Na Deposition on MnO(100)

Xu Feng, David F. Cox<sup>\*</sup>

Department of Chemical Engineering, Virginia Polytechnic Institute and State University, Blacksburg, VA 24061, United States



## ARTICLE INFO

### Article history:

Received 4 August 2015

Accepted 25 October 2015

Available online 31 October 2015

### Keywords:

Sodium

Manganese oxide

Temperature programmed desorption

X-ray photoelectron spectroscopy

Stranski–Krastanov growth

Density functional theory

## ABSTRACT

Na deposition on the MnO(100) surface was investigated by temperature programmed desorption (TPD), X-ray photoelectron spectroscopy (XPS) and low energy electron diffraction (LEED). Na TPD and XPS results indicate that adsorbed Na interacts strongly with the MnO substrate to form an irreversibly-adsorbed, oxidic Na compound on the surface for coverages up to 1 monolayer (ML). This strongly-bound Na diffuses into the MnO subsurface and bulk at elevated temperatures above 500 K. For Na coverages above 1 ML, metallic Na is present and desorbs from the surface below 500 K. The deposition of Na on MnO(100) follows a Stranski–Krastanov (SK) growth mode, with the formation of metallic Na islands following completion of the first Na monolayer. After Na deposition, the surface exhibits a diffuse ( $1 \times 1$ ) LEED pattern, suggesting the formation of disordered Na overlayers. After heating to 1000 K, the surface presents a ( $2 \times 2$ ) LEED pattern indicating that a surface reconstruction is induced by the diffusion of Na into the near surface region. CO<sub>2</sub> can be used as a probe molecule in TPD to distinguish between metallic Na islands and oxidic Na in the first ML, and to indicate when Na that is still observable by XPS goes subsurface.

© 2015 Elsevier B.V. All rights reserved.

## 1. Introduction

Xu, Bhawe and Davis recently reported a low-temperature, manganese-oxide-based, catalytic thermochemical water splitting cycle [1]. The shuttling of Na<sup>+</sup> into and out of manganese oxides was determined to be a key factor to drive the water splitting cycle below 1000 °C. These observations provide a motivation for studying the interaction of Na with manganese oxide surfaces and any corresponding solid state reactions.

Alkali-metal-promoted, rocksalt-structured metal oxides have found applications in heterogeneous catalysis for chemistry such as the oxidative coupling of methane [2–6], oxidative dehydrogenation of ethane [5, 7], DeSO<sub>x</sub> [8–10], water gas shift [11] and soot combustion [12]. Studies of interactions between alkali metals and rocksalt-structured metal oxides are essential to understand the fundamental properties of these alkali-metal-promoted catalytic surfaces. From a surface science perspective, a number of alkali metal/rocksalt-structured metal oxide surface combinations have been investigated, such as Na on NiO(111) [13], Na/K on NiO(100) [14–16], Li/Na/K on Ni(110)–O [17–19], Na/K/Cs on MgO(100) [20–25], Na on MgO(111) [21], and Na on CaO(100) [8,10]. To the best of our knowledge, no study of interactions between alkali metals and the rocksalt-structured MnO has been reported.

In this work, Na deposition on MnO(100) was studied for various Na coverages. Temperature programmed desorption (TPD) and X-ray photoelectron spectroscopy (XPS) were used to characterize the forms of deposited Na, and CO<sub>2</sub> TPD was used as a probe to further distinguish

different forms of surface Na. Low energy electron diffraction (LEED) was also used to monitor variations of the surface periodicity. A Stranski–Krastanov (SK) growth mechanism for Na deposition on MnO(100) is proposed.

## 2. MnO(100)

Fig. 1 shows a ball model illustration of an ideal stoichiometric MnO(100) surface, with atom sizes referenced to Mn and O bonded radii [26]. Bulk MnO has a rocksalt structure which is the simplest oxide structure [27]. In the bulk, each Mn<sup>2+</sup> cation is surrounded by six equidistant O<sup>2−</sup> anions, while each O<sup>2−</sup> anion is surrounded by six equidistant Mn<sup>2+</sup> cations. The crystal structure of MnO can be considered as the insertion of two fcc lattices of Mn<sup>2+</sup> and O<sup>2−</sup> ions [28]. The non-polar MnO(100) surface has the lowest surface energy among all the low miller-index surfaces, and is thermodynamically stable [27]. An ideal (100) surface exposes an atomically flat plane containing equal numbers of Mn<sup>2+</sup> cations and O<sup>2−</sup> anions with a square periodicity (a:b = 1:1), however in practice, surface defects such as steps or missing ions cannot be avoided [27]. The clean MnO(100) surface shows very little rumpling or reconstruction in the ultra-high vacuum environment [29,30].

## 3. Methods

### 3.1. Experimental methods

All experiments were carried out in a turbo-pumped, dual-chamber, stainless steel ultra-high vacuum (UHV) system. The preparation

<sup>\*</sup> Corresponding author.

E-mail address: [dfcox@vt.edu](mailto:dfcox@vt.edu) (D.F. Cox).

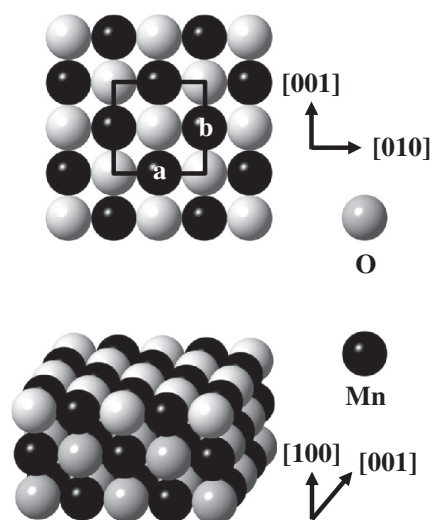


**Fig. 1.** Ball model illustration of the ideal stoichiometric MnO(100) surface. Gray spheres represent  $\text{O}^{2-}$  anions, and black spheres represent  $\text{Mn}^{2+}$  cations. Atom sizes are referenced to Mn and O bonded radii [26]. Surface  $\text{O}^{2-}$  anions on the (100) plane are marked with lighter gray color for clarity. The top picture shows the surface periodicity ( $a:b = 1:1$ ) looking down the [100] surface normal. The bottom picture shows a cross-section view along the [001] direction.

chamber with a base pressure of  $2 \times 10^{-10}$  Torr is equipped with a Leybold IQE 10/35 ion gun, a set of Princeton Research Instruments reverse view LEED optics and an Inficon Quaqrex 200 mass spectrometer for TPD. The analysis chamber with a base pressure of  $1 \times 10^{-10}$  Torr is equipped with a Leybold EA-11 hemispherical analyzer and a Mg K $\alpha$  radiation source for XPS, and a Na evaporator with an SAES getter as the Na source.

The MnO(100) single crystal was purchased from SurfaceNet GmbH with an EPI polish. The sample was mechanically clamped onto a Ta stage that was fastened to LN<sub>2</sub>-cooled copper electrical feedthroughs in a sample rod manipulator. The sample temperature was directly measured by a type K thermocouple attached to the back of the single crystal through a hole in the Ta stage using Aremco 569 ceramic cement. The sample can be resistively heated to 1000 K and LN<sub>2</sub>-cooled to 125 K. A heating rate of  $2.5 \text{ K s}^{-1}$  was used in TPD. The low heating rate was used to avoid thermal-induced fracture of the ceramic MnO sample.

Na was evaporated onto the sample from a resistively heated Na SAES getter placed approximately 30 mm away from the sample.  $^{13}\text{CO}_2$  (Sigma-Aldrich, 99 atom %  $^{13}\text{C}$ , < 3 atom %  $^{18}\text{O}$ ) was used as received.  $^{13}\text{CO}_2$  was introduced by backfilling the chamber through a variable leak valve, and exposures have been corrected for an ion gauge sensitivity of 1.4 [31].

XPS spectra were acquired at 60 eV pass energy for Mn, O and Na 1 s which gives a Ag 3d<sub>5/2</sub> line width of 1.06 eV, and 200 eV pass energy for Na KLL which gives a Ag 3d<sub>5/2</sub> line width of 2.1 eV. All binding energies have been referenced to an O 1 s binding energy of 530.1 eV for the MnO(100) substrate using an approach similar to that of Langell et al. [30]. This value was obtained with the sample at an elevated temperature of 473 K which provides sufficient conductivity to eliminate surface charging. Reported values for XPS Na/Mn ratios are determined from the integrated intensity of the Na 1 s and Mn 2p photoemission features following satellite and Shirley background [32] subtraction. All XPS ratios have been corrected with Leybold atomic sensitivity factors *except where noted*. All XPS spectra shown in this work have been corrected by satellite subtraction but no background corrections have been applied.

All reported LEED patterns utilize a beam energy of 90 eV, and were collected at elevated temperatures high enough to provide sufficient conductivity to avoid surface charging. For surfaces with multilayer coverages of Na, a temperature of 350 K is sufficient to prevent charging,

with no thermally-induced chemical change as verified by XPS. For other surfaces, a temperature of 473 K was used.

A clean and nearly-stoichiometric MnO(100) surface was prepared by ion bombardment at elevated temperature ( $\text{Ar}^+$  bombardment, 2 KeV, 1000 K) and annealing to 1000 K in UHV. For the cleaning procedure, ion bombardment was begun with the sample at 300 K, the temperature was raised to 1000 K in the ion beam, and then the sample was cooled back to 300 K in the ion beam before the annealing process. We note that after multiple Na doses, it was found that low temperature (300 K) ion bombardment could produce a Na-free disordered MnO(100) surface (as determined by XPS), but subsequent 1000 K annealing in UHV to order the surface always resulted in a detectable amount of Na in the surface region due to the outward diffusion of Na from the bulk at high temperatures, thereby necessitating the use of ion bombardment at elevated temperatures in the sample preparation process. After the preparation procedure, the sample exhibits a sharp ( $1 \times 1$ ) LEED pattern characteristic of a simple termination of the rocksalt-structured (cubic) MnO bulk. This surface gives a Mn 2p<sub>3/2</sub> binding energy of 641.0 eV, with a satellite feature at 6.2 eV higher binding energy. Both values are in good agreement with previous reports for a clean and stoichiometric MnO(100) surface [30]. A Mn 3 s splitting of 6.1 eV is observed, which also agrees with values reported for MnO [33–39]. XPS gives an *uncorrected* O 1 s to Mn 2p intensity ratio of 0.24, which matches the value for a clean and stoichiometric MnO(100) surface reported by Langell et al. [30].

### 3.2. Computational methods

DFT has been used to examine the preferred adsorption site for Na on MnO(100). All calculations were performed using the projector-augmented-wave method [40,41] within the Vienna Ab-initio Simulation Package (VASP) [42–44]. The Perdue–Burke–Ernzerhof (PBE) approximation was used to treat exchange and correlation utilizing a standard generalized gradient approximation (GGA) [45]. A 256 atom cell was used that exposed a ( $4 \times 4$ ) surface mesh with a thickness of four atomic layers along [100]. Following optimization of the bulk structure, a 15 Å vacuum gap was introduced, and the atoms in the bottom atomic layer were fixed at the bulk positions. A  $1 \times 3 \times 3$  k-point sampling based on the Monkhorst–Pack scheme [46] was used. For all calculations, the initial magnetic moments of the  $\text{Mn}^{2+}$  cations ( $d^3$ ) were set following the known AFM-II antiferromagnetic ordering in MnO [47], which is also found to be the ground-state magnetic ordering for DFT within the GGA [48]. A 400 eV cut-off energy was used throughout. For all geometry optimized structures, the forces on the individual atoms are less than 0.01 eV/Å.

In addition to PBE, PBE + U in the form proposed by Dudarev et al. [49] has been used to examine the Na adsorption site. Two values of  $U$ – $J$ , 4.0 eV and 6.0 eV, have been examined. Following the work of Franchini et al. [50] for bulk MnO and Bayer et al. [51] for MnO(100), the value of  $U$ – $J = 6.0$  eV is optimal for MnO based on consideration of the band gap, the spin magnetic moment,  $e_g - t_{2g}$  splitting, and the lattice parameter, while a value of 4.0 eV yields the best energy of formation for MnO [48,52]. To examine charge transfer in these systems, Bader's Atoms-in-Molecules [53] approach has been used to determine atomic charges using the implementation of Henkelman and coworkers [54–56].

## 4. Results and discussion

### 4.1. Na TPD

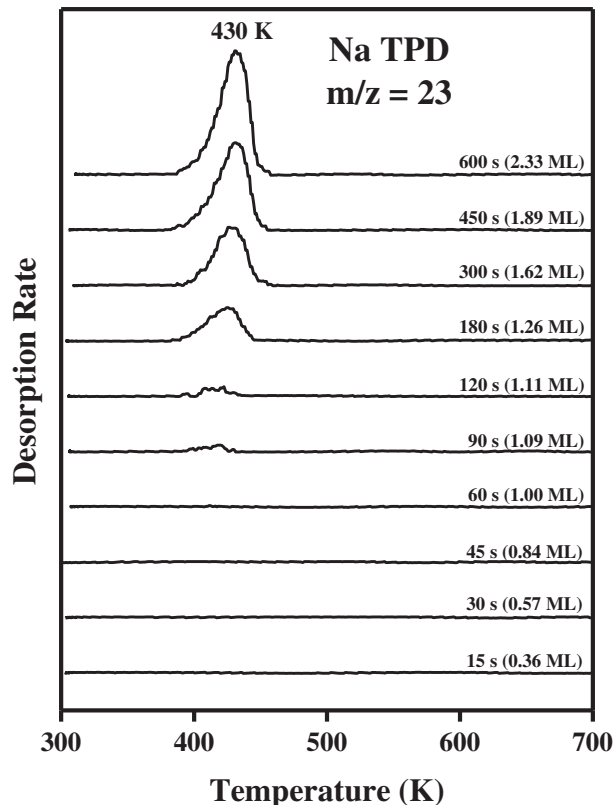
Na TPD was used to characterize energetically-different bound forms of Na on MnO(100). Before each Na deposition, a clean and nearly-stoichiometric MnO(100) surface was prepared. The surface then was exposed to Na vapor at a sample temperature of 300 K, and TPD was run for the temperature range from 300 K to 1000 K.

Fig. 2 shows the TPD traces of Na ( $m/z = 23$ ) from MnO(100) with increasing Na deposition time and coverage. (The method used to determine Na coverage is given in Fig. 3 and described in Section 4.2.1.) For Na deposition times up to 60 s (1 ML), no Na desorption feature is observed. No other Na-related products such as  $\text{Na}_2\text{O}$  ( $m/z = 62$ ), NaOH ( $m/z = 40$ ) or Na–O fragments ( $m/z = 39$ ) are detected. These results indicate that for coverages up to 1 ML, Na is irreversibly adsorbed. For a Na deposition time of 90 s (1.09 ML), a single Na desorption feature appears in the temperature range from 385 to 430 K, indicating that a second form of Na with weaker binding to the surface is present for coverages exceeding 1 ML. For increasing Na deposition times, this feature grows with a common leading edge, but shifts to higher peak temperatures with increasing coverage, suggesting a zeroth-order desorption process [57]. The activation energy of this zeroth-order desorption is estimated by an Arrhenius analysis of the leading edge data [57] as  $116 \text{ kJ mol}^{-1}$ , which is close to the heat of sublimation of metallic Na ( $108 \text{ kJ mol}^{-1}$ ) [28]. Similarly, a Na desorption feature near 400 K was reported for the desorption of a metallic Na multilayer from Au(111) [58]. In summary, two forms of Na are indicated: (1) irreversibly-adsorbed Na for coverages up to 1 ML, and (2) metallic Na above 1 ML coverage which desorbs near 430 K.

## 4.2. XPS study of Na deposition on MnO(100)

### 4.2.1. Na growth mode

Fig. 3 shows a plot of the Na 1s/Mn 2p XPS intensity ratio as a function of Na deposition time. The Na/Mn ratio increases linearly with increasing Na deposition time until a break point is observed for a Na dosing time of about 60 s. For Na exposures beyond 60 s, the Na/Mn ratio increases linearly, but with a lower slope. This growth behavior matches the Stranski–Krastanov (SK) growth mode [59], which can be



**Fig. 2.** TPD traces of Na ( $m/z = 23$ ) following Na deposition on the clean and nearly-stoichiometric MnO(100) surface with increasing Na deposition time (coverage). The coverage calibration is discussed in Section 4.2.1. Na is irreversibly-adsorbed up to 1 ML coverage, and metallic Na desorbs below 500 K above 1 ML coverage.

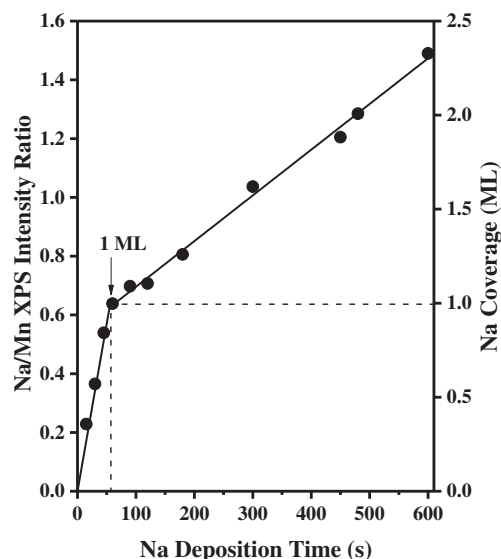


**Fig. 3.** Na 1s/Mn 2p XPS intensity ratio (left ordinate) and Na coverage (right ordinate) as a function of Na deposition time. 1 ML Na coverage occurs at the break point near 60 s of Na exposure following the Stranski–Krastanov (SK) growth mode description.

described as the completion of a Na monolayer followed by island formation. A similar growth mode was reported for Na adsorption on MgO(111) [21] and K adsorption on NiO(100) [15]. Following the SK growth mode description, the break point near 60 s of Na exposure ( $\text{Na/Mn} = 0.64$ ) can be used as a phenomenological indicator of 1 ML Na coverage. Applying a linear correlation between the Na/Mn XPS intensity ratio and the break point associated with 1 ML gives the ML coverage scale on the right hand side of Fig. 3.

### 4.2.2. XPS spectra of deposited Na

XPS was used to characterize the Na chemical states arising from Na deposition on MnO(100). Before each Na deposition, a clean and nearly-stoichiometric MnO(100) surface was prepared. The surface was maintained at 300 K during Na deposition, and XPS spectra were collected at 300 K after deposition.

Fig. 4 shows the Na 1s and Na KLL XPS spectra for Na on MnO(100) at various coverages. No Na signal is detected for the clean MnO(100) surface. In the Na 1s XPS spectra, a Na 1s peak appears at 1072.2 eV for a 0.36 ML Na coverage. For Na coverages up to 1 ML, the Na 1s binding energy remains fairly constant, indicating that the Na chemical state is nominally constant within the first monolayer. For higher Na coverages above 1 ML, the Na 1s binding energy shifts to lower values. At 2.33 ML Na coverage, the Na 1s binding energy has shifted down by 0.7 eV to 1071.5 eV. At this point, two plasmon loss features are apparent at binding energies 5.7 eV and 11.4 eV higher than that of Na 1s, indicating the presence of metallic Na [13,21,60,61]. The variation of the Na 1s binding energy with increasing Na coverage is highlighted in Fig. 5. Compared to the 1s binding energy of metallic Na, the 0.7 eV higher binding energy in the first monolayer matches the difference between  $\text{Na}_2\text{O}$  and metallic Na [8,21,61], suggesting that the Na in the first monolayer interacts strongly with the MnO substrate, resulting in the formation of an oxidic Na compound. Similar observations have been reported for Na deposition on several other rocksalt-structured metal oxides, such as MgO(111) [21] and CaO(100) [8,10]. For MgO and CaO, the formation of  $\text{Na}_2\text{O}$  within the first monolayer [8,14,21], followed by the buildup of metallic Na [8,20,21] was suggested. These reports are in agreement with our results for Na on MnO(100).

A more significant variation with increasing Na coverage is observed in the Na KLL Auger features in Fig. 4. At 0.36 ML Na coverage, a single Na KLL peak at 263.9 eV is present, suggesting the formation of a Na surface compound [13,60–62]. For increasing Na coverages up to 1 ML, this

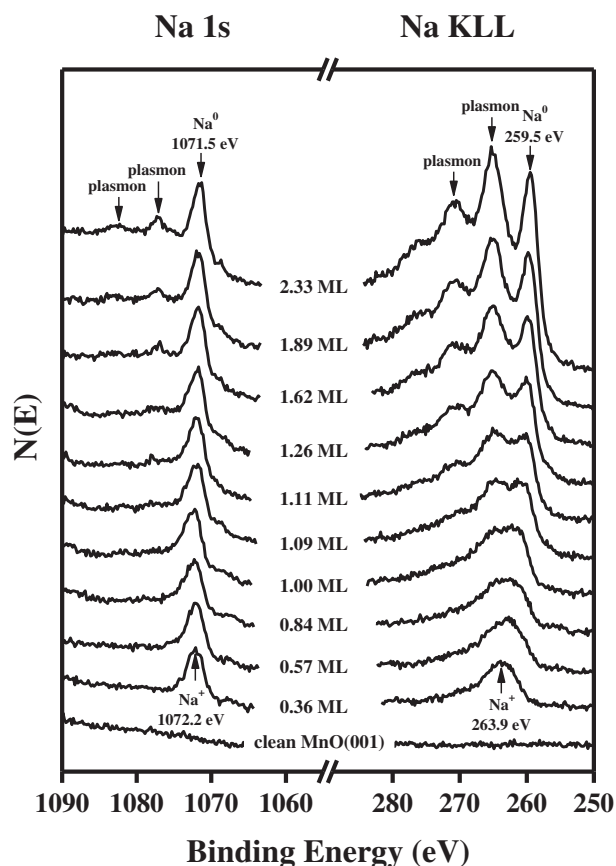


Fig. 4. Na 1s and Na KLL XPS spectra of Na on MnO(100) at various coverages. An oxidic Na compound is formed up to 1 ML coverage, and metallic Na builds up for coverages above 1 ML.

feature broadens. At 1 ML coverage, this signal shows evidence of a split into two separate features. A third feature at lower binding energy becomes apparent at 1.11 ML coverage, and all three features continue to grow for higher Na coverages. At 2.33 ML Na coverage, three peaks are well resolved: the Na KLL at 259.5 eV, and two plasmon loss features at binding energies 5.7 eV and 11.4 eV higher than that of Na KLL which are characteristic of metallic Na [13,60,61]. Compared to the KLL binding energy of metallic Na, the 4.4 eV increase for the Na compound matches

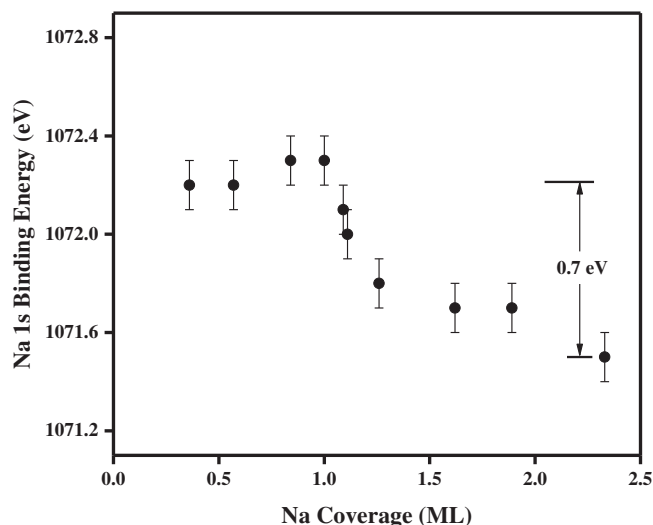


Fig. 5. Na 1s binding energy as a function of Na coverage.

the reported 4.5 eV difference of Na KLL binding energy between Na<sub>2</sub>O and metallic Na [61], suggesting again the formation of an oxidic Na compound within the first monolayer. These results are consistent with the Na 1s results described above, and the Na KLL features appear to give a more sensitive indication of the appearance of metallic Na characterized by intense plasmon loss features. In summary, two Na chemical states are present during Na deposition on MnO(100): oxidic Na within the first ML, and metallic Na at higher coverages.

The Na XPS and Na TPD results support the previously proposed SK growth mode of Na deposition on MnO(100). For Na coverages up to 1 ML, Na interacts strongly with the MnO substrate to form an irreversibly-adsorbed, oxidic Na compound, followed by the formation of metallic Na islands for coverages above 1 ML.

#### 4.2.3. XPS spectra of Mn and O

Mn and O XPS signals were also examined in an attempt to probe Na binding site preferences on MnO(100). Mn and O XPS spectra were acquired in the same measurements along with the Na XPS spectra discussed above.

Fig. 6 shows the Mn 2p<sub>3/2</sub>, Mn 3s and O 1s XPS spectra of Na on MnO(100) for various Na coverages. With increasing Na coverage, both Mn 2p<sub>3/2</sub> and Mn 3s signal intensities decrease due to the deposition of Na. However, no obvious differences are observed in other characteristics of the XPS signals such as peak width (FWHM), giving no indication of a change in Mn chemical state. For the rocksalt-structured metal oxide NiO, there are several reports of the partial reduction of Ni<sup>2+</sup> cations to Ni<sup>0</sup> metal upon interactions with alkali metals (Li [18, 19], Na [13,18,19] and K [16–19]), although similar reductions are not reported for Na on MgO(100) [21] or CaO(100) [8,10]. In this work, Mn<sup>2+</sup> reduction to Mn<sup>0</sup> is not observed. Similar to the observations

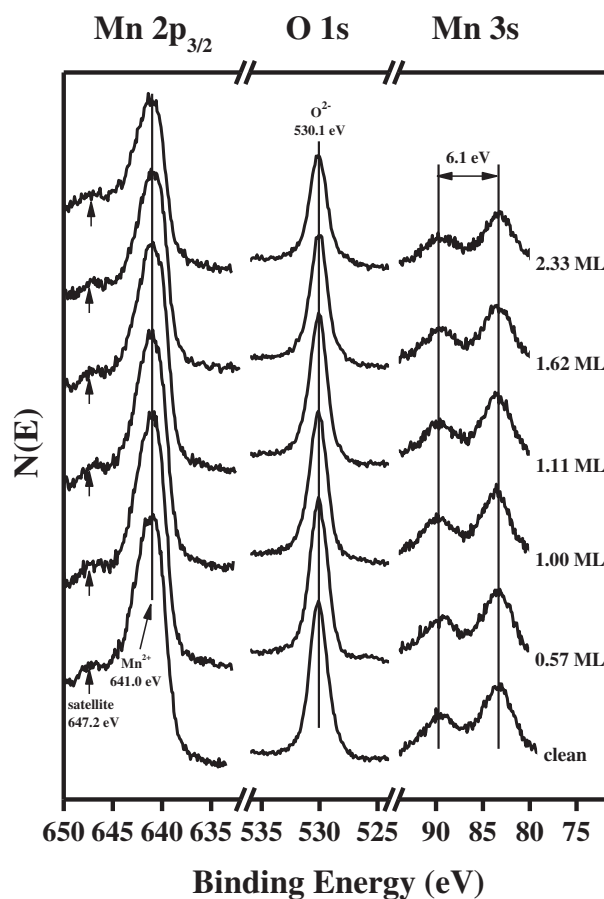


Fig. 6. Mn 2p<sub>3/2</sub>, Mn 3s and O 1s XPS spectra of Na on MnO(100) at various coverages. No clear indication of Na binding preference to the MnO substrate is observed.

for Mn, the O 1 s features also exhibit attenuated intensities with increasing Na coverage but are essentially unchanged in width and position relative to the O 1 s signal from the clean surface. Hence, the XPS results for Mn and O provide no clear indication of the preferred Na binding sites on the MnO substrate. Nonetheless, the Na 1 s binding energy for sub-monolayer coverages of Na (Section 4.2.2) indicates the involvement of surface O atoms to form an oxidic Na surface compound.

#### 4.2.4. XPS spectra of thermally-treated Na

Na XPS was used to investigate thermally-induced changes in deposited Na. Two surfaces were prepared for this study: surface (a) with an initial 0.36 ML Na coverage associated with irreversibly-adsorbed, oxidic Na, and surface (b) with an initial 1.26 ML Na coverage exhibiting both irreversibly-adsorbed and metallic Na. For each surface, Na XPS measurements were performed after Na deposition at 300 K, after heating to 500 K (above the temperature where Na desorption is observed in TPD), and after heating to 1000 K.

Fig. 7a shows the Na 1s and Na KLL XPS spectra for surface (a) with an initial 0.36 ML Na coverage associated with irreversibly-adsorbed Na. After heating to 500 K, Na 1 s binding energy remains nominally unchanged, suggesting no change in Na chemical state. While, the Na 1 s peak is sharper after heating, the peak areas are nominally constant, indicating some minor nonuniformity in the Na deposited at 300 K. This difference shows up as a small shoulder on the higher binding energy side for the as-deposited Na. Similarly the Na KLL feature also appears sharper after heating to 500 K. These results are consistent with the Na TPD and Na XPS results, indicating that the surface concentration of Na in the first monolayer does not change for heating to temperatures up to 500 K. After further heating to 1000 K, there is a significant

decrease of the Na signal intensities compared to those after heating to 500 K. Given that Na desorption is not observed in TPD above 500 K, the results indicate that irreversibly-adsorbed Na in the first monolayer diffuses into the MnO bulk and near-surface region at temperatures between 500 and 1000 K.

Fig. 7b shows the Na 1 s and Na KLL XPS spectra for surface (b) with an initial 1.26 ML Na coverage exhibiting both irreversibly-adsorbed and metallic Na. After Na deposition, metallic Na is present with characteristic plasmon loss features in both Na 1 s and Na KLL spectra. After heating to 500 K, the plasmon loss features characteristic of metallic Na disappear, indicating that metallic Na is no longer present. This result coincides with the temperature range where the Na TPD desorption feature at 430 K is observed, leading to the conclusion that the Na desorption feature at 430 K in TPD is associated with metallic Na sublimation. XPS signals of the irreversibly-adsorbed Na remaining after heating to 500 K attenuate after heating to 1000 K, also suggesting that Na in the first monolayer diffuses into the MnO subsurface and bulk, similar to the observations for surface (a).

#### 4.3. LEED study of Na deposition on MnO(100)

LEED was used to characterize surface periodicity of clean and Na-covered MnO(100). Four surfaces were prepared: (a) the clean and nearly-stoichiometric MnO(100) surface; (b) a surface with 1.26 ML Na coverage exhibiting both irreversibly-adsorbed and metallic Na as in Fig. 7b; (c) the surface in (b) heated to 500 K and exhibiting only irreversibly-adsorbed Na in the first monolayer with no metallic Na; and (d) the surface in (c) heated to 1000 K where irreversibly-adsorbed Na has diffused into the near surface region and MnO bulk. As shown in Fig. 8, surface (b) with both irreversibly-adsorbed and metallic Na exhibits a more diffuse ( $1 \times 1$ ) LEED pattern compared to the sharper ( $1 \times 1$ ) pattern of the clean surface (a), suggesting some disorder in the Na overlayers. Surface (c) exhibiting only irreversibly-adsorbed Na with no metallic Na also exhibits a diffuse ( $1 \times 1$ ) LEED pattern similar to surface (b), again suggesting some disorder in the

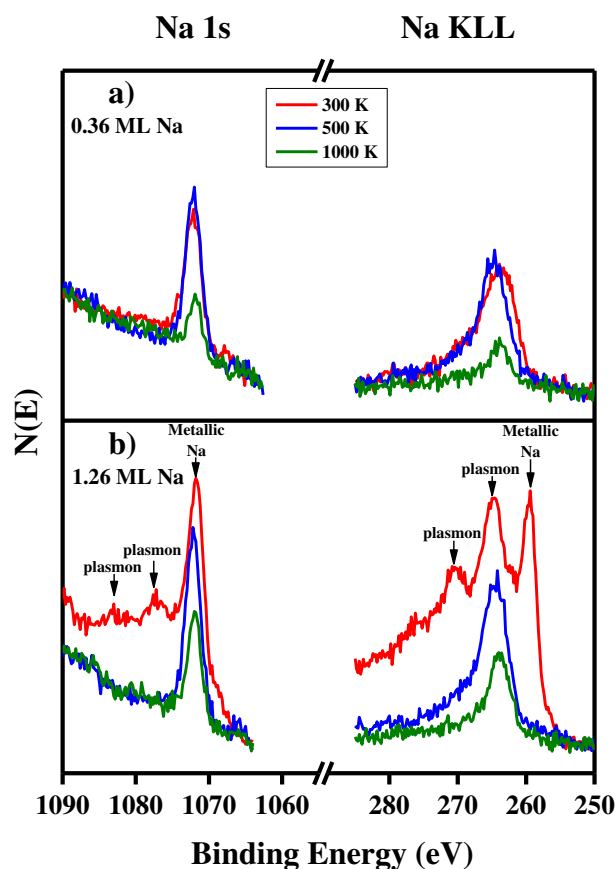


**Fig. 7.** Na 1s and Na KLL XPS spectra of Na on MnO(100) for initial coverages of 0.36 ML (exhibiting only irreversibly-adsorbed, oxidic Na in the first monolayer) and 1.26 ML (exhibiting both irreversibly-adsorbed and metallic Na) at 300 K, after heating to 500 K, and heating to 1000 K.

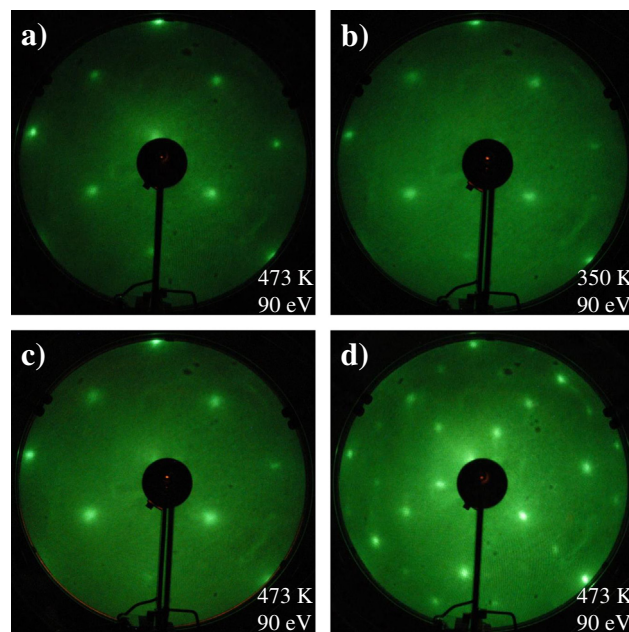


**Fig. 8.** LEED patterns of (a) the clean and nearly-stoichiometric MnO(100) surface; (b) the MnO(100) surface with 1.26 ML Na coverage exhibiting both irreversibly-adsorbed, oxidic Na in the first monolayer and metallic Na; (c) the MnO(100) surface with initial 1.26 ML Na coverage heating to 500 K to remove metallic Na, and exhibiting only irreversibly-adsorbed, oxidic Na in the first monolayer; (d) the MnO(100) surface with initial 1.26 ML Na coverage heating to 1000 K, where irreversibly-adsorbed Na has diffused into the MnO subsurface and bulk.

Na distributed within the first monolayer. The surface in Fig. 8d exhibits a  $(2 \times 2)$  LEED pattern after heating to 1000 K, indicating a surface reconstruction is associated with the inward diffusion of Na to subsurface sites at temperatures between 500 and 1000 K.

We note that our LEED observations differ from others in the literature. Langell and Cameron [63] reported a preparation procedure where 2 keV  $\text{Ar}^+$  bombardment followed by annealing at 650 K in  $5 \times 10^{-7}$  Torr of  $\text{O}_2$  was used to give a reproducible surface composition and a  $(1 \times 1)$  LEED periodicity. Extended thermal annealing in UHV at 800 K gave rise to a  $(2 \times 2)$  surface reconstruction, with a  $(6 \times 6)$  periodicity obtained by heating to 1000 K. They note that varying levels of Ca segregate to their surface during annealing, and that the amount of Ca contamination can impact the temperatures required to drive the reconstructions. We have repeated their preparation procedures (2 keV  $\text{Ar}^+$  bombardment, annealing in  $\text{O}_2$ , followed by prolonged UHV annealing) and fail to see any reconstructions when our XPS characterization suggests a clean near-surface composition. We only observe a  $(2 \times 2)$  reconstruction in the presence of Na in subsurface sites. We feel it is likely that the Ca contamination in their study played a similar role to the Na in our study, with the Ca contamination being responsible for the observed reconstructions.

#### 4.4. DFT simulation of surface Na

DFT was used to simulate the binding of Na at low coverage for insight into the preferred binding site on flat  $\text{MnO}(100)$ . For both the PBE and the PBE + U simulations, the low energy binding site is found to be associated with a surface O anion, in agreement with the XPS results which suggests an oxidic character to the Na atoms within the first monolayer. Fig. 9 shows the predicted structures for one Na atom. While both methods predict O anion binding sites, the binding geometry varies greatly. Fig. 9(a) and (b) show the local geometry of the adsorption site for PBE and PBE + U ( $U-J = 6.0$  eV), respectively, while the impact of Na on the underlying surface layer is illustrated in Fig. 9(c) and (d) for PBE and PBE + U ( $U-J = 6.0$  eV), respectively. Results for  $U-J = 4.0$  eV give structures indistinguishable from those for  $U-J = 6.0$  eV illustrated in Fig. 9(b) and (d). Adsorption energies, Na–O bond lengths, and changes in the Na atom Bader charges due to adsorption are given in Table 1. In all cases, the adsorption energies are exothermic and the change in Bader charge suggests a partial positive charge on the adsorbed Na compared to a neutral free Na

**Table 1**  
DFT predictions for atomic Na adsorption on  $\text{MnO}(100)$ .

	Na adsorption energy (eV)	Na–O bond length (Å)	$\Delta$ Na atom Bader charge on adsorption ( <i>e</i> )
PBE	−2.739	2.28	+0.63
PBE + U ( $U-J = 4$ )	−0.589	2.32	+0.47
PBE + U ( $U-J = 6$ )	−0.560	2.32	+0.44

atom, indicating charge transfer from Na to the surface. The changes are consistent with the identification of oxidic Na in the first monolayer in XPS.

For the PBE calculations, a single Na atom drives a  $(2 \times 2)$  reconstruction of the top atomic layer of  $\text{MnO}(100)$  across the full  $(4 \times 4)$  surface mesh. This reconstruction is *not* observed with DFT + U, where a simple atop configuration is found for Na with a Na–O bond length of 2.32 Å. Note that while experimentally a  $(2 \times 2)$  reconstruction was observed with LEED for Na in *subsurface* sites, irreversibly adsorbed Na in the first monolayer exhibits a  $(1 \times 1)$  periodicity. For this system, PBE + U gives a structural prediction more in line with experiment.

#### 4.5. $^{13}\text{CO}_2$ TPD

$\text{CO}_2$  was used as a probe molecule to further distinguish the different forms of surface Na. Fig. 10 shows the TPD traces of  $^{13}\text{CO}_2$  ( $m/z = 45$ ) for several different surface treatments. For each TPD trace, the surface was cooled to 125 K, then exposed to 0.5 L ( $1 \text{ L} = 1 \times 10^{-6} \text{ Torr} \cdot \text{s}$ ) of  $^{13}\text{CO}_2$  for TPD. For clean  $\text{MnO}(100)$  in Fig. 10a,  $^{13}\text{CO}_2$  desorbs primarily

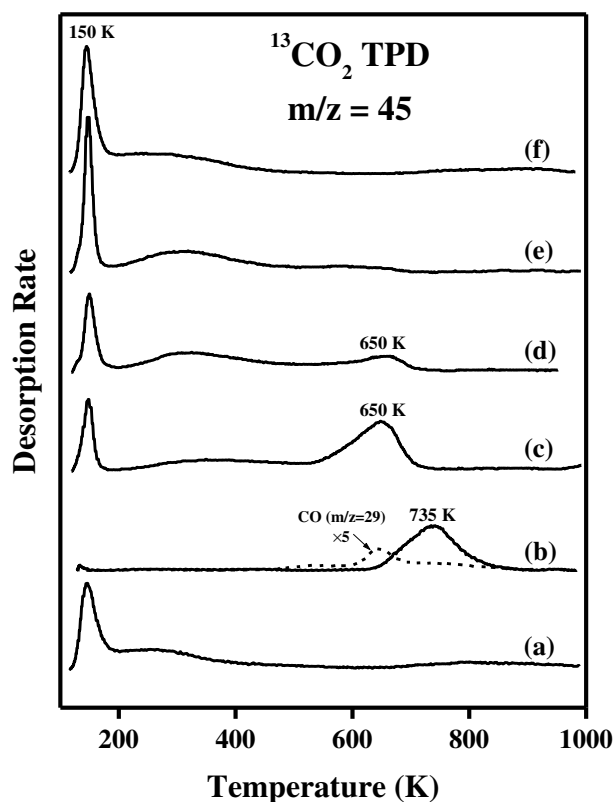


**Fig. 10.** TPD traces of  $^{13}\text{CO}_2$  ( $m/z = 45$ ) following 0.5 L  $^{13}\text{CO}_2$  adsorption on: (a) the clean and nearly-stoichiometric  $\text{MnO}(100)$  surface; (b) the  $\text{MnO}(100)$  surface with 2.33 ML Na coverage dominated by metallic Na; (c) the  $\text{MnO}(100)$  surface with an initial 1.26 ML Na coverage heated briefly to 500 K to remove metallic Na, and exhibiting only irreversibly-adsorbed, oxidic Na in the first monolayer; (d) the  $\text{MnO}(100)$  surface with an initial 1.26 ML Na coverage heated briefly to 600 K; (e) the  $\text{MnO}(100)$  surface with an initial 1.26 ML Na coverage heated to 600 K for 10 min; (f) the  $\text{MnO}(100)$  surface with an initial 1.26 ML Na coverage heated briefly to 1000 K.

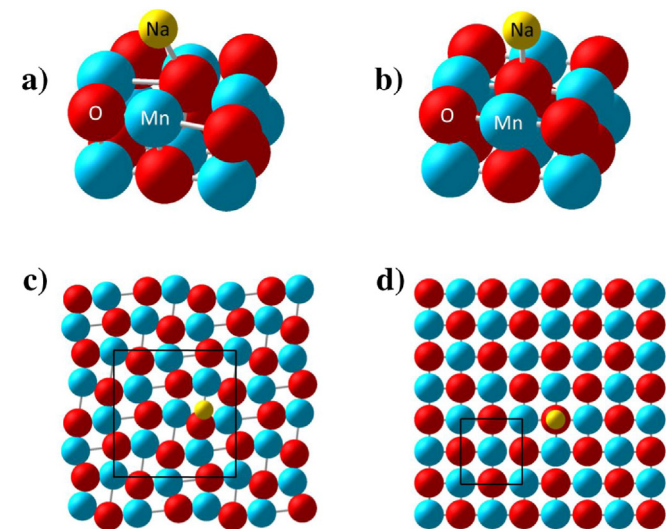


**Fig. 9.** DFT binding site of Na on  $\text{MnO}(100)$ . In the low coverage limit, the preferred Na binding site is atop surface O anions, with a Na–O bond length of 2.32 Å predicted by PBE + U.

below 200 K with a peak at 150 K and a minor broad desorption feature in the range of 200–400 K, suggesting that CO<sub>2</sub> interacts relatively weakly with MnO(100) in the absence of Na. In Fig. 10b on the surface with a 2.33 ML Na coverage dominated by metallic Na, a high temperature <sup>13</sup>CO<sub>2</sub> desorption feature at 735 K is observed, indicating that CO<sub>2</sub> interacts much more strongly with this surface than the clean MnO(100) due to a strong binding with metallic Na. A broad <sup>13</sup>CO signal is also observed between 450 K and 800 K indicating a disproportionation reaction of strongly adsorbed CO<sub>2</sub> on metallic sodium [64]: 2NaCO<sub>2</sub> → Na<sub>2</sub>CO<sub>3</sub> + CO. Less than 20% of the adsorbed CO<sub>2</sub> is estimated to go through the disproportionation reaction to form Na<sub>2</sub>CO<sub>3</sub>, indicating that the majority of the <sup>13</sup>CO<sub>2</sub> desorption feature originates from chemisorbed CO<sub>2</sub> on Na. (The intensities of the CO and CO<sub>2</sub> traces in Fig. 10b have been corrected for relative mass spectrometer sensitivity factors, and the CO signal has been corrected for contributions from the CO<sub>2</sub> fragmentation pattern.) In Fig. 10c, a surface exposing only irreversibly adsorbed Na gives a <sup>13</sup>CO<sub>2</sub> desorption feature at 650 K with no <sup>13</sup>CO desorption, indicating that CO<sub>2</sub> also interacts strongly with oxidic Na in the first monolayer, but more weakly than with metallic Na. The different binding strengths of CO<sub>2</sub> clearly distinguishes the two different forms of Na. Heating a surface similar to that in Fig. 10c briefly to 600 K gives rise to the trace in Fig. 10d. The 650 K CO<sub>2</sub> desorption feature at 650 K is significantly attenuated, indicating that a temperature of 600 K is sufficient to activate the thermally-induced diffusion of a significant fraction of the Na into the subsurface. Holding the temperature at 600 K for 10 min (Fig. 10e) is sufficient to drive the majority of Na in the first monolayer into the subsurface where it is no longer accessible to the CO<sub>2</sub> adsorbent. Heating to 1000 K (Fig. 10f), results in a CO<sub>2</sub> TPD trace similar to that from the clean surface, indicating that the remaining Na observed in XPS following similar treatments has all been driven subsurface.

## 5. Conclusion

Na deposition on the MnO(100) surface follows the Stranski–Krastanov (SK) growth mode with two forms of Na identified. Up to 1 ML Na coverage, Na is randomly distributed on the MnO(100) surface before the completion of the monolayer and interacts strongly with the MnO substrate, binding in an oxidic form. This form of Na is irreversibly-adsorbed and diffuses into the MnO bulk at elevated temperatures above 500 K. For Na coverages above 1 ML, metallic Na islands nucleate and grow on top of the Na monolayer. Metallic Na desorbs from the surface at 430 K.

## Acknowledgment

The authors gratefully acknowledge financial support by the Chemical Sciences, Geosciences and Biosciences Division, Office of Basic Energy Sciences, Office of Science, U.S. Department of Energy through Grant DE-FG02-97ER14751, and private support from Mr. and Mrs. Lewis W. van Amerongen. The authors also acknowledge Advanced Research Computing at Virginia Tech for providing computational resources and technical support that have contributed to the results reported within this paper.

## Appendix A. Supplementary data

Supplementary data to this article can be found online at <http://dx.doi.org/10.1016/j.susc.2015.10.041>.

## References

- [1] B. Xu, Y. Bhawe, M.E. Davis, Proc. Natl. Acad. Sci. 109 (2012) 9260.
- [2] J.G. Chen, M.D. Weisel, J.H. Hardenbergh, F.M. Hoffmann, C.A. Mims, R.B. Hall, J. Vac. Sci. Technol. A 9 (1991) 1684.
- [3] E. Iwamatsu, T. Moriyama, N. Takasaki, K. Aika, J. Catal. 113 (1988) 25.
- [4] E. Iwamatsu, K.-I. Aika, J. Catal. 117 (1989) 416.
- [5] A. Machocki, A. Denis, Chem. Eng. J. 90 (2002) 165.
- [6] D.J. Wang, M.P. Rosynek, J.H. Lunsford, J. Catal. 155 (1995) 390.
- [7] H.M. Swaan, A. Toebes, K. Seshan, J.G. van Ommen, J.R.H. Ross, Catal. Today 13 (1992) 201.
- [8] Y.C. Lee, P.A. Montano, J.M. Cook, Surf. Sci. 143 (1984) 423.
- [9] J.A. Rodriguez, M. Pérez, T. Jirsak, L. González, A. Maiti, Surf. Sci. 477 (2001) L279.
- [10] R.V. Siriwardane, J.M. Cook, J. Colloid Interface Sci. 114 (1986) 525.
- [11] R.W. Stevens Jr., A. Shamsi, S. Carpenter, R. Siriwardane, Fuel 89 (2010) 1280.
- [12] R. Jiménez, X. García, C. Cellier, P. Ruiz, A.L. Gordon, Appl. Catal. A Gen. 297 (2006) 125.
- [13] M. Bender, K. Al-Shamery, H.J. Freund, Langmuir 10 (1994) 3081.
- [14] T. Rogelet, S. Söderholm, M. Qvarford, N.L. Saini, U.O. Karlsson, I. Lindau, S.A. Flodström, Solid State Commun. 85 (1993) 657.
- [15] S. Kennou, M. Kamaratos, C.A. Papageorgopoulos, Vacuum 41 (1990) 22.
- [16] M. Schulze, R. Reissner, Surf. Sci. 507–510 (2002) 851.
- [17] A.F. Carley, S.D. Jackson, J.N. O'Shea, M.W. Roberts, Surf. Sci. 440 (1999) L868.
- [18] A.F. Carley, S.D. Jackson, M.W. Roberts, J. O'Shea, Surf. Sci. 454–456 (2000) 141.
- [19] A.F. Carley, S.D. Jackson, J.N. O'Shea, M.W. Roberts, Phys. Chem. Chem. Phys. 3 (2001) 274.
- [20] T. Kendelewicz, P. Liu, G.E. Brown Jr., E.J. Nelson, P. Pianetta, Surf. Sci. 352–354 (1996) 451.
- [21] H. Onishi, C. Egawa, T. Aruga, Y. Iwasawa, Surf. Sci. 191 (1987) 479.
- [22] H.H. Huang, X. Jiang, Z. Zou, G.Q. Xu, Surf. Sci. 376 (1997) 245.
- [23] H.H. Huang, X. Jiang, Z. Zou, G.Q. Xu, W.L. Dai, K.N. Fan, J.F. Deng, Surf. Sci. 398 (1998) 203.
- [24] H.H. Huang, X. Jiang, H.L. Siew, W.S. Chin, G.Q. Xu, Surf. Sci. 418 (1998) 320.
- [25] H.H. Huang, X. Jiang, Z. Zou, W.S. Chin, G.Q. Xu, W.L. Dai, K.N. Fan, J.F. Deng, Surf. Sci. 412–413 (1998) 555.
- [26] G.V. Gibbs, N.L. Ross, D.F. Cox, K.M. Rosso, B.B. Iversen, M.A. Spackman, J. Phys. Chem. A 117 (2013) 1632.
- [27] V.E. Henrich, P.A. Cox, The Surface Science of Metal Oxides, Cambridge University Press, Cambridge, NY, 1994.
- [28] N.N. Greenwood, A. Earnshaw, Chemistry of the Elements, 2nd ed. Elsevier, 1997.
- [29] M. Prutton, J.A. Walker, M.R. Welton-Cook, R.C. Felton, J.A. Ramsey, Surf. Sci. 89 (1979) 95.
- [30] M.A. Langell, C.W. Hutchings, G.A. Carson, M.H. Nassir, J. Vac. Sci. Technol. A 14 (1996) 1656.
- [31] R.L. Summers, NASA Technical Note TN D-5285, Washington, D. C., 1969.
- [32] D.A. Shirley, Phys. Rev. B 5 (1972) 4709.
- [33] V. Di Castro, G. Polzonetti, J. Electron Spectrosc. Relat. Phenom. 48 (1989) 117.
- [34] F. Müller, R. de Masi, D. Reinicke, P. Steiner, S. Hüfner, K. Stöwe, Surf. Sci. 520 (2002) 158.
- [35] L.Z. Zhao, V. Young, J. Electron Spectrosc. Relat. Phenom. 34 (1984) 45.
- [36] J.S. Foord, R.B. Jackman, G.C. Allen, Philos. Mag. A Phys. Condens. Matter Struct. Defect Mech. Prop. 49 (1984) 657.
- [37] M. Oku, K. Hirokawa, S. Ikeda, J. Electron Spectrosc. Relat. Phenom. 7 (1975) 465.
- [38] C.S. Fadley, D.A. Shirley, Phys. Rev. A 2 (1970) 1109.
- [39] P. Steiner, R. Zimmermann, F. Reinert, T. Engel, S. Hüfner, Z. Phys. B: Condens. Matter 99 (1996) 479.
- [40] P.E. Blöchl, Phys. Rev. B 50 (1994) 17953.
- [41] G. Kresse, D. Joubert, Phys. Rev. B 59 (1999) 1758.
- [42] G. Kresse, J. Furthmüller, Phys. Rev. B 54 (1996) 11169.
- [43] G. Kresse, J. Furthmüller, Comput. Mater. Sci. 6 (1996) 15.
- [44] G. Kresse, J. Hafner, Phys. Rev. B 47 (1993) 558.
- [45] J.P. Perdew, K. Burke, M. Ernzerhof, Phys. Rev. Lett. 77 (1996) 3865.
- [46] H.J. Monkhorst, J.D. Pack, Phys. Rev. B 13 (1976) 5188.
- [47] H. Shaked, J. Faber, R.L. Hitterman, Phys. Rev. B 38 (1988) 11901.
- [48] C. Franchini, R. Podloucky, J. Paier, M. Marsman, G. Kresse, Phys. Rev. B 75 (2007) 195128.
- [49] S.L. Dudarev, G.A. Botton, S.Y. Savrasov, C.J. Humphreys, A.P. Sutton, Phys. Rev. B 57 (1998) 1505.
- [50] C. Franchini, V. Bayer, R. Podloucky, J. Paier, G. Kresse, Phys. Rev. B 72 (2005) 045132.
- [51] V. Bayer, C. Franchini, R. Podloucky, Phys. Rev. B 75 (2007) 035404.
- [52] L. Wang, T. Maxisch, G. Ceder, Phys. Rev. B 73 (2006) 195107.
- [53] R.F.W. Bader, Atoms in Molecules: A Quantum Theory, New York, Oxford University Press, New York, 1990.
- [54] G. Henkelman, A. Arnaldsson, H. Jonsson, Comput. Mater. Sci. 36 (2006) 354.
- [55] E. Sanville, S.D. Kenny, R. Smith, G. Henkelman, J. Comput. Chem. 28 (2007) 899.
- [56] W. Tang, E. Sanville, G. Henkelman, J. Phys. Condens. Matter 21 (2009) 7.
- [57] D.A. King, T.E. Madey, J.T. Yates, J. Chem. Phys. 55 (1971) 3247.
- [58] J.V. Barth, R.J. Behm, G. Ertl, Surf. Sci. 341 (1995) 62.
- [59] J.A. Venables, G.D.T. Spiller, M. Hanbucken, Rep. Prog. Phys. 47 (1984) 399.
- [60] J.F. Moulder, W.F. Stickle, P.E. Sobol, K.D. Bomben, Handbook of X-ray Photoelectron Spectroscopy, Perkin-Elmer Corporation, Eden Prairie, MN, 1992.
- [61] A. Barrie, F.J. Street, J. Electron Spectrosc. Relat. Phenom. 7 (1975) 1.
- [62] C.D. Wagner, W.M. Riggs, L.E. Davis, J.F. Moulder, G.E. Muilenberg, Handbook of X-ray Photoelectron Spectroscopy, Perkin-Elmer Corporation, Eden Prairie, MN, 1978.
- [63] M.A. Langell, N.R. Cameron, Surf. Sci. 185 (1987) 105.
- [64] O. Seiferth, K. Wolter, H. Kühlenbeck, H.J. Freund, Surf. Sci. 505 (2002) 215.